

# Reactive orange 12 dye adsorption onto magnetically separable $\text{CaFe}_2\text{O}_4$ nanoparticles synthesized by simple chemical route: kinetic, isotherm and neural network modeling

Payel Das and Animesh Debnath 

Department of Civil Engineering, National Institute of Technology Agartala, Jirania, West Tripura 799046, India

\*Corresponding author. E-mail: debnathanimesh@gmail.com

 AD, 0000-0001-9008-3070

## ABSTRACT

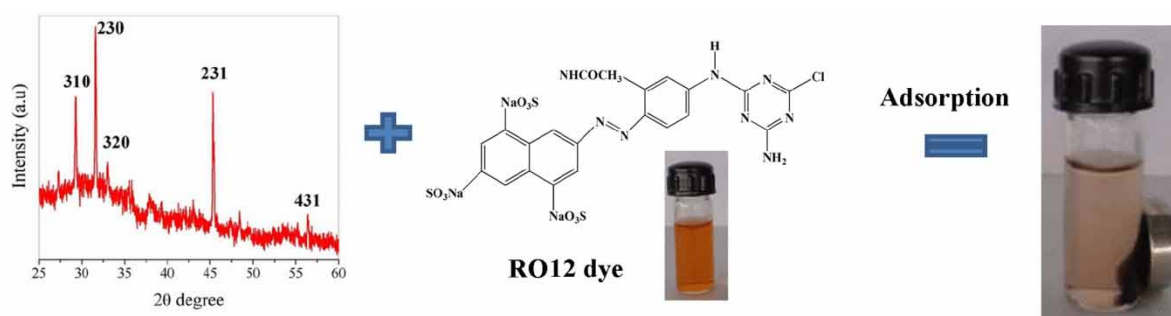
Industrial wastewaters laden with toxic dyes are required to be treated prior to their disposal in view of their adverse effect on human health and aquatic ecosystems. Thus in this research,  $\text{CaFe}_2\text{O}_4$  nanoparticles were prepared and used as adsorbent for elimination of reactive orange 12 dye (RO12) from aqueous medium. The  $\text{CaFe}_2\text{O}_4$  nanoparticles exhibit specific surface area of  $\sim 230 \text{ m}^2/\text{g}$  and average pore diameter of  $\sim 2.5 \text{ nm}$ . Maximum RO12 removal of 77% was observed at solution pH 2.0 with uptake capacity of 276.92 mg/g. The electrostatic interaction between  $\text{CaFe}_2\text{O}_4$  nanoparticles and RO12 was the main driving force behind this adsorption. The kinetic modeling reveals that this adsorption process obeyed the pseudo-second-order kinetic model accurately ( $R^2$ : 0.988–0.994), indicating chemisorption behavior. The adsorption experimental data firmly followed the Langmuir isotherm model ( $R^2$ : 0.997), confirming monolayer adsorption. Thermodynamic study suggests that the adsorption process is spontaneous ( $\Delta G^0 = -8.76$  to  $-3.19 \text{ kJ/mol}$ ) and exothermic in nature ( $\Delta H^0 = -71.86 \text{ kJ}$ ). A neural network model (optimum topology of 4–7–1) was developed for precise forecasting of RO12 removal (%). The developed model with very high correlation coefficient (0.986) and very low mean squared error (0.00185) was successful for accurate prediction of experimental data.

**Key words:** adsorption, dye, kinetic study, magnetic nanoparticle, neural network modeling

## HIGHLIGHTS

- The nano size of  $\text{CaFe}_2\text{O}_4$  helps achieving good adsorption capacity of 276.92 mg/g.
- The adsorption procedure follows pseudo-second order kinetics and the Langmuir isotherm model.
- ANN model shows very high correlation coefficient ( $R^2 = 0.986$ ) and very low mean squared error ( $\text{MSE} = 0.00185$ ).
- Magnetically separable  $\text{CaFe}_2\text{O}_4$  nanoparticles are easy to separate from aqueous media due to their superior magnetic property.

## GRAPHICAL ABSTRACT



This is an Open Access article distributed under the terms of the Creative Commons Attribution Licence (CC BY 4.0), which permits copying, adaptation and redistribution, provided the original work is properly cited (<http://creativecommons.org/licenses/by/4.0/>).

## 1. INTRODUCTION

Effluents from industries like textile, paper, rubber, food coloring, cosmetics and so on are loaded with large amounts of toxic dyes, which on disposal to water bodies may cause serious water pollution (Gupta *et al.* 2012; Chen *et al.* 2014; Asim *et al.* 2019). Dye-burdened wastewater may increase the chemical oxygen demand of water and reduce light penetration and photosynthesis activity of the water bodies. Some dyes are non-biodegradable owing to their complex aromatic structure, and carcinogenic as well as mutagenic to human beings (Bhowmik *et al.* 2016; Deb *et al.* 2017; Bhowmik *et al.* 2018). The toxic effects of these synthetic dyes have encouraged the environmental scientists to search for novel techniques or materials for their safe and effective removal from water. Therefore, several physical, chemical, and microbiological approaches such as chemical oxidation/precipitation, photo-degradation, coagulation, microbiological degradation and so on have been utilized to treat dye-loaded wastewater (Chafi *et al.* 2011; Cui *et al.* 2012; Debnath & Chakraborty 2013; Debnath *et al.* 2015). Among several dye remediation methods, adsorption is one of the most effective techniques due to the availability of a large number of adsorbents, easy operation, high efficiency, and economic feasibility. A wide variety of adsorbents like activated carbon, industrial waste, agricultural waste, zeolites, clays, and polymers have been testified for removal of dyes from water (Deng *et al.* 2013; Yao *et al.* 2014; Zeng *et al.* 2014; Montoya-suarez *et al.* 2016; Bhowmik *et al.* 2017; Bhowmik *et al.* 2019). But many of them suffer from low adsorption capacity, high cost, poor regeneration ability, slow adsorption rate and so on. Furthermore, separation of adsorbents from heterogeneous systems is another serious drawback that restricts their large-scale industrial wastewater treatment applications (Liu *et al.* 2012; Hajati *et al.* 2014).

Magnetic metal ferrite nanoparticles have attracted a lot of interest as an adsorbent for eradicating dyes, heavy metals, and other water contaminants from aqueous systems (Li *et al.* 2011; Khanna & Verma 2013). Additionally, metal ferrites are also known for their enhanced photo-catalytic properties for degradation of organic water pollutants (Al-Anzari *et al.* 2018, 2020). Nano adsorbents are normally preferred owing to their small size, high surface area and large pore volume, which provide faster adsorption and high adsorption capacity compared to the traditional adsorbents. Moreover, nano adsorbents with magnetic properties can provide extra nuance owing to their facile separation from water, resulting in easy recyclability and lower operational cost. Several magnetically separable metal ferrite nanoparticles such as  $\text{ZnFe}_2\text{O}_4$ ,  $\text{MnFe}_2\text{O}_4$ ,  $\text{MgFe}_2\text{O}_4$ , and  $\text{CoFe}_2\text{O}_4$  have been used as adsorbent for remediation of dyes like Congo red, Crystal violet, and Acid red 88 (Konicki *et al.* 2013; Liu *et al.* 2015; He *et al.* 2017; Singh *et al.* 2018). Liu *et al.* (2015) reported the removal of Congo red dye by  $\text{MnFe}_2\text{O}_4$  with maximum adsorption capacity of 41.99 mg/g. Similarly, Singh *et al.* (2018) reported the removal of Crystal violet dye by  $\text{CoFe}_2\text{O}_4$  nanoparticles with maximum adsorption capacity of 105 mg/g. He *et al.* (2017) described the removal of Congo red dye by  $\text{MgFe}_2\text{O}_4$  and maximum adsorption capacity was found to be ~76 mg/g. Konicki *et al.* (2013) reported the successful application of  $\text{ZnFe}_2\text{O}_4$  for Acid red 88 dye with maximum adsorption capacity of 111.1 mg/g. However, adsorption studies on reactive dyes by magnetic spinel ferrite nanoparticles have not yet been explored properly. Reactive orange 12 (RO12) is a reactive anionic dye and commonly used for biological staining, coloring cellulosic textiles, dermatology and veterinary medicine. In addition to toxicity towards ecosystems, human toxicity of RO12 includes skin cancer, permanent eye injury and so on, but reports on removal/degradation of RO12 are scanty (Ghaedi *et al.* 2014; Fraga *et al.* 2018). Thus in this research, the adsorptive potential of magnetic  $\text{CaFe}_2\text{O}_4$  nanoparticles was evaluated for removal of RO12, as the  $\text{CaFe}_2\text{O}_4$  nanoparticles are expected to be more biocompatible compared to other ferrites owing to its non-toxicity and environmentally friendly nature (Khanna & Verma 2014). Furthermore, due to high chemical and mechanical stability, and easy magnetic separation owing to its super paramagnetic behavior,  $\text{CaFe}_2\text{O}_4$  nanoparticles could be a potential candidate as an adsorbent for large-scale application (Berchmans *et al.* 2010).

Thus the main objective of this research is to explore the potential of  $\text{CaFe}_2\text{O}_4$  nanoparticles for adsorptive uptake of RO12 dye from an aqua matrix. The  $\text{CaFe}_2\text{O}_4$  nanoparticles were fabricated using a facile precipitation method and characterized extensively for its crystalline structure, surface morphology, active chemical bonds on its surface, specific surface area, and magnetic behavior. Effects of various experimental parameters like solution pH,  $\text{CaFe}_2\text{O}_4$  nanoparticle dose, reaction time, and initial RO12 concentrations onto the RO12 uptake (%) were investigated thoroughly. Kinetic and isotherm modeling studies were performed with adsorption experimental data to find the insights of the adsorption process. Moreover, to explore the effect of reaction temperature on the adsorption process of RO12 onto  $\text{CaFe}_2\text{O}_4$  nanoparticles, the thermodynamic study was also performed

and important thermodynamic parameters were assessed. Finally, a three-layer feed-forward neural network model was established using adsorption experimental data for accurate prediction of RO12 removal (%).

## 2. MATERIALS AND METHODS

### 2.1. Chemicals and reagents

Analytical grade calcium chloride dihydrate ( $\text{CaCl}_2 \cdot 2\text{H}_2\text{O}$ ), NaOH pellets and ferric chloride anhydrous ( $\text{FeCl}_3$ ) were bought from Merck, (India). RO12 powder ( $\text{C}_{20}\text{H}_{23}\text{ClN}_9\text{O}_{10}\text{S}_3\text{Na}$ ; 739.98 g/mol) was obtained from Leo chem Pvt. Ltd (India). Ultrapure deionized (DI) water (Millipore) was utilized throughout the experiment.

### 2.2. Fabrication and characterization of $\text{CaFe}_2\text{O}_4$ nanoparticles

In a typical experiment, 20.0 g of NaOH pellets was dissolved in 500 mL of DI water and agitated until the solution turned translucent. In the following step,  $\text{FeCl}_3$  (12.0 g) and  $\text{CaCl}_2 \cdot 2\text{H}_2\text{O}$  (12.0 g) were dissolved in 250 mL DI water separately in two beakers and stirring was continued till both the solutions became transparent. Thereafter,  $\text{FeCl}_3$  and  $\text{CaCl}_2 \cdot 2\text{H}_2\text{O}$  solutions were added gently to the NaOH solution and mixed until a brownish precipitate was achieved. Following the reaction, the precipitate was filtered and dried in an oven at  $85^\circ\text{C}$  for 12 hours. The obtained precursor was then cleaned several times with DI water to eliminate unreacted impurities. The properly washed precursor was then heated at  $200^\circ\text{C}$  for 8 hours in a muffle furnace. Finally, the brown solid materials were ground and  $\text{CaFe}_2\text{O}_4$  was obtained in powder form and used for RO12 dye adsorption studies (Deb *et al.* 2017).

An X-ray diffractometer (Bruker, D-8 Advance) was used to measure the X-ray diffraction (XRD) pattern of  $\text{CaFe}_2\text{O}_4$  powder for  $2\theta$  values from  $20^\circ$  to  $70^\circ$  with  $\text{Cu K}_\alpha$  radiation ( $\lambda = 1.54178^\circ\text{A}$ ). The crystallite domain size was calculated from the width of the XRD peaks using the Scherrer's formula.

$$D = \frac{0.9\lambda}{\beta \cos \theta} \quad (1)$$

In Equation (1), 'D' represents the average crystallite domain size perpendicular to the reflecting planes,  $\lambda$  represents the X-ray wavelength,  $\beta$  represents the full width at half maximum (FWHM), and  $\theta$  is the diffraction angle. Morphological investigation was performed by field emission scanning electron microscope (FESEM, Hitachi, S-4800). The Fourier transform infrared (FTIR) spectrum of  $\text{CaFe}_2\text{O}_4$  powder was recorded with FTIR spectrometer (Perkin Elmer). The transmission electron microscopy (TEM) measurement were carried out by transmission electron microscope (JEOL, 200 kV HRTEM). The Brunauer-Emmett-Teller (BET) analysis was performed using automated gas sorption system IQ-C nitrogen adsorption apparatus (Quanta-chrome Autosorb). A vibrating sample magnetometer (VSM) (Lakeshore, 7410 series) was used to investigate the magnetic characteristics of  $\text{CaFe}_2\text{O}_4$  powder. The salt addition method was used to analyze the PZC of  $\text{CaFe}_2\text{O}_4$  nanoparticles. A succession of 100 mL test tubes holding 20 mL of 0.01 M KCl solution were adjusted to a pH range of 2.0–10.0 in this method. This pH was reported as the initial pH (pHi). Aqueous 0.1 N HCl or 0.1 N NaOH was used to modify the pH of these samples.  $\text{CaFe}_2\text{O}_4$  nanoparticles in a controlled amount (0.02 g) were introduced to each tube. The solutions were well mixed and kept undisturbed for 48 hours. The filtrates' final pHs (pHf) were then measured after the solutions were separated. The pH change from pHi to pHf ( $\Delta\text{pH}$ ) was plotted against pHi, and the pHi value at which the pH is zero shows the adsorbent's PZC (Caner *et al.* 2015).

### 2.3. Batch adsorption experiments

A certain amount of adsorbent was added to 50 mL of dye solution, and the mixture was stirred for a fixed time using an overhead stirrer at 200 rpm. The adsorbent was extracted from the dye solution using an external magnetic field after the completion of reaction and the supernatant was analyzed for residual dye concentration using a UV-Vis-NIR spectrophotometer (Shimadzu UV-3101PC) at maximum absorbency of RO12 ( $\lambda_{\text{max}} = 415\text{ nm}$ ).

Experiments were conducted to investigate the consequence of initial solution pH on the RO12 uptake efficiency in the 2.0–7.0 pH range at room temperature. During the above mentioned experiments, the initial RO12 concentration and  $\text{CaFe}_2\text{O}_4$  nanoparticles dose were maintained at 100 mg/L, and 1.0 g/L, respectively and the reaction was continued up to 80 min. The variation of RO12 removal and adsorption capacity in relation to  $\text{CaFe}_2\text{O}_4$  nanoparticles dose was explored over the  $\text{CaFe}_2\text{O}_4$  dose of 0.125–1.5 g/L. This effect of  $\text{CaFe}_2\text{O}_4$  dose study was performed with initial RO12 concentration of 80 mg/L, contact time of 80 min and solution

pH of 2.0. The variation of RO12 dye uptake efficiency (%) and adsorption capacity (mg/g) as a function of initial RO12 dye concentration with fixed  $\text{CaFe}_2\text{O}_4$  nanoparticles dose (1.0 g/L) was performed for RO12 dye concentration (20.0–150.0 mg/L). The initial RO12 concentration was varied from 20–80 mg/L at a fixed  $\text{CaFe}_2\text{O}_4$  nanoparticle dose of 1.0 g/L for studying the effect of contact time.

## 2.4. Adsorption kinetic analysis, isotherm modeling and thermodynamic studies

The adsorption kinetic models are used to assess the contribution and inspection of mass transfer mechanisms in any adsorption process. In the adsorption kinetic modeling, the experimental data of RO12 onto  $\text{CaFe}_2\text{O}_4$  nanoparticles were fitted to the linear form of three kinetics models, namely the pseudo-first-order, pseudo-second-order and intra-particle diffusion models. The correlation coefficient ( $R^2$ ) value was used to designate the favorable kinetic model, which ascertains the adsorption type; that is, physical adsorption or chemisorption process. The intra-particle diffusion model exhibits the mass transfer process as well as the interaction among dye and the active sites of the adsorbent. The experimental data were obtained by varying the initial RO12 concentration (20–80 mg/L) with fixed  $\text{CaFe}_2\text{O}_4$  nanoparticles dose (1.0 g/L) for adsorption kinetic studies. The adsorption isotherm models provide the information about the maximum adsorption capacity of the adsorbent and the type of adsorption. Thus the adsorption isotherm analysis was conducted by Langmuir and Freundlich isotherm model. Langmuir isotherm describes the chemisorption process with monolayer distribution of adsorbate onto the adsorbent; however, the Freundlich isotherm model defines the heterogeneous adsorption with multilayer physical adsorption process. Adsorption equilibrium experiments were performed at room temperature, varying the initial dye concentration (20–150 mg/L) with fixed  $\text{CaFe}_2\text{O}_4$  nanoparticles dose of 1.0 g/L for isotherm studies. The effect of temperature on this adsorption process was explored by thermodynamic study. In thermodynamic study, the experiments were conducted at five different temperatures in the range of 27 °C to 55 °C using  $\text{CaFe}_2\text{O}_4$  dose 1.0 g/L, contact time 80 min, and at the RO12 concentration of 60 mg/L.

## 2.5. Artificial neural network (ANN) modeling

Artificial neural network (ANN) is a popular mathematical tool that was developed based on the idea of biological neurons. This prediction tool is found to be quite effective for the accurate forecasting of output variables in chemical process modeling. The foremost benefit of the ANN tool lies in its capacity to deliver precise modeling for non-linear models having multiple inputs. Moreover, ANN tool also find its wide application due to its capacity to deal with inconsistent and unreliable data with its ability of fault tolerance and sturdiness (Kooch *et al.* 2016). Considering the above, the ANN tool was used to predict the RO12 removal (%) using the adsorption experimental data. In this study, ANN based modeling was executed by the neural network tool box of MATLAB 8.0.0.783 (R2012a) software for prediction of RO12 removal (%). A three layer feed forward back propagation network was developed with ‘tansig’ and ‘purelin’ functions at hidden and output layer, respectively. For network training, the Levenberg-Marquardt (LM) algorithm with 1,000 epochs was implemented. Four experimental parameters i.e. solution pH, initial RO12 concentration (mg/L), contact time (min), and  $\text{CaFe}_2\text{O}_4$  dose (g/L) were selected as input parameters and 1 – 30 neurons were varied in the hidden layer to obtain the optimal network based on the minimum value of mean squared error (MSE) and maximum value of coefficient of determination ( $R^2$ ). MSE and  $R^2$  can be exemplified by Equations (2) and (3), respectively.

$$MSE = \frac{1}{N} \sum_{i=1}^N (|y_{prd,i} - y_{exp,i}|)^2 \quad (2)$$

$$R^2 = 1 - \frac{\sum_{i=1}^N (y_{prd,i} - y_{exp,i})}{\sum_{i=1}^N (y_{prd,i} - y_m)} \quad (3)$$

In Equations (2) and (3),  $y_{prd,i}$  and  $y_{exp,i}$  represent the projected and experimental value, respectively; the parameter ‘N’ indicates the number of data points and  $y_m$  is the average of all the experimental data. Before utilizing in the network training, all the input as well as output experimental data were normalized within 0.0 to 1.0 using Equation (4), and a total of 174 data points were divided randomly into training, testing and validation sets with

70, 15 and 15% data points, respectively (Kumari *et al.* 2015; Pirouz *et al.* 2015).

$$X_{norm} = \frac{(X - X_{min})}{(X_{max} - X_{min})} \quad (4)$$

In Equation (4),  $X_{norm}$ ,  $X_{max}$ , and  $X_{min}$  are the normalized, maximum, and minimum value of variable X.

The weightage of four considered input parameters on the output parameter was computed using Equation (5) (Bhowmik *et al.* 2020).

$$R = \frac{\sum_{j=1}^h \left[ \left( \frac{|IW_{ij}|}{\sum_{k=1}^m |IW_{kj}|} \right) |LW_j| \right]}{\sum_{j=1}^m \left\{ \sum_{j=1}^h \left[ \left( \frac{|IW_{ij}|}{\sum_{k=1}^m |IW_{kj}|} \right) LW_j \right] \right\}} \quad (5)$$

where,  $R$  is the weightage of the input variable  $x$ ,  $m$  and  $h$  are the number of neurons in the input and hidden layer, respectively.

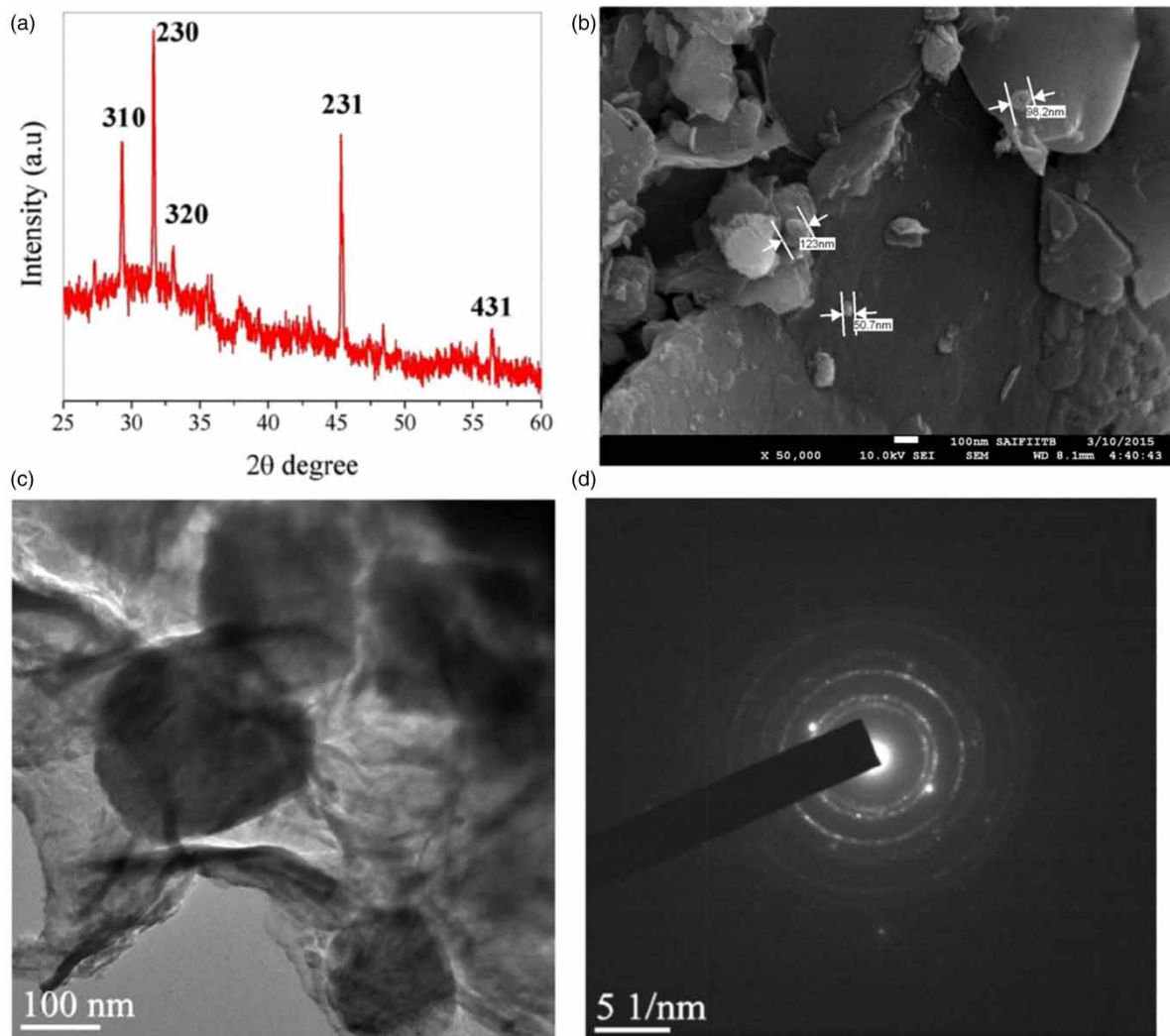


**Figure 1** | (a) XRD pattern; (b) FESEM image; (c) TEM micrograph and (d) selected area diffraction pattern of  $\text{CaFe}_2\text{O}_4$  nanoparticles.



### 3. RESULTS AND DISCUSSION

#### 3.1. Characterization of $\text{CaFe}_2\text{O}_4$ nanoparticles

XRD pattern of the synthesized  $\text{CaFe}_2\text{O}_4$  nanoparticles (Figure 1(a)) was analyzed to explore its crystallinity and phase components. The significant peaks occurred in the XRD pattern due to the reflection from (310), (230), (320), (201), (221), (400), (231), (340), (331), and (431) Miller planes of  $\text{CaFe}_2\text{O}_4$  (Deb *et al.* 2017). The average crystallite domain size of the synthesized nanoparticles was computed using Figure 1(a) and was found  $\sim 37$  nm. A FESEM image was captured to understand the surface morphology of  $\text{CaFe}_2\text{O}_4$  nanoparticles, which is depicted in Figure 1(b). The FESEM image shows the particle size distribution throughout a range, with the average size being less than 100 nm. Because of the material's paramagnetic properties, some particle aggregation was observed in the FESEM image. The TEM micrograph of synthesized  $\text{CaFe}_2\text{O}_4$  nanoparticles is shown in Figure 1(c), which also indicates almost similar size distribution of the particles, likewise FESEM. The crystalline phases of the  $\text{CaFe}_2\text{O}_4$  nanoparticles were established by the selected area diffraction pattern (Figure 1(d)), which correlates with the XRD pattern.

FTIR spectroscopy was accomplished to understand the available surface bonding of  $\text{CaFe}_2\text{O}_4$  nanoparticles, which is depicted in Figure 2(a). Several active surface bonds were found in the FTIR spectrum in the range of  $4,000 - 400 \text{ cm}^{-1}$ , which confirmed the availability of active functional groups on the surface the synthesized nanomaterial. The detailed description of all the significant peaks observed in the FTIR spectrum is illustrated

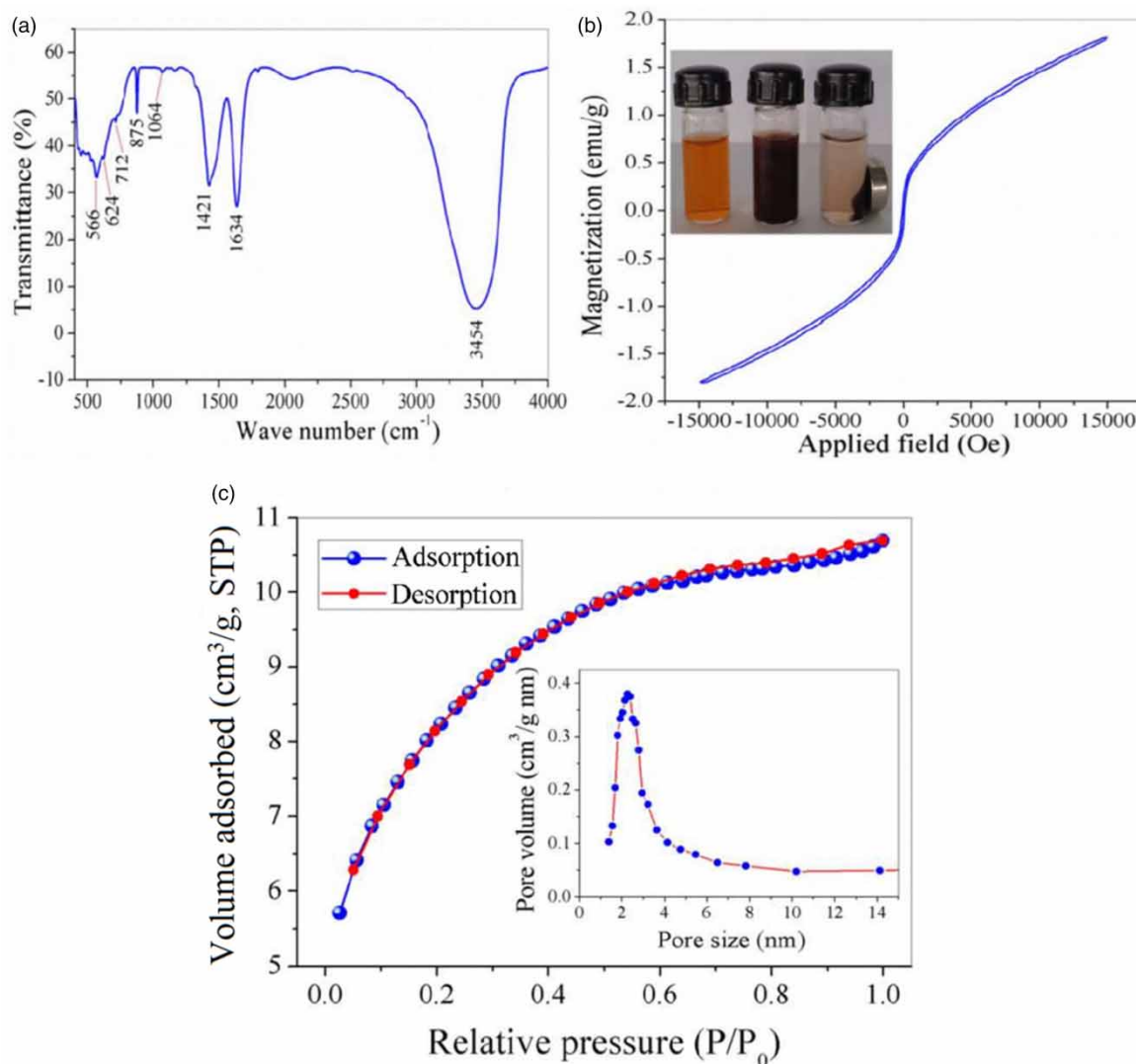


**Figure 2** | (a) FTIR spectrum; (b) VSM magnetization curve and efficient magnetic separation of  $\text{CaFe}_2\text{O}_4$  nanoparticles (inset); and (c)  $\text{N}_2$  adsorption/desorption isotherm and pore volume distribution (inset) of  $\text{CaFe}_2\text{O}_4$  nanoparticles.

in Table 1. The magnetic response of the  $\text{CaFe}_2\text{O}_4$  nanoparticles was studied by VSM measurements in the magnetic field of  $-15\text{ K}$  to  $+15\text{ K Oe}$ . The sample is found to be super-paramagnetic, with a magnetic saturation ( $M_s$ ) value of  $1.82\text{ emu/g}$  (Figure 2(b)). The sample's remanent magnetization ( $M_R$ ) and squareness value ( $M_R/M_s$  ratio) are  $0.13\text{ emu/g}$  and  $0.071$ , respectively. The super paramagnetic behavior of the sample is confirmed from the squareness value (less than  $0.1$ ), which means the synthesized nanoparticles are magnetizable in manifestation of an external magnetic field, permitting faster and simpler separation from aqueous solution (Yang *et al.* 2014). The photo showing the efficient separation of  $\text{CaFe}_2\text{O}_4$  nanoparticles using a magnet is shown in Figure 2(b) (inset). The  $\text{N}_2$  gas adsorption-desorption isotherm of  $\text{CaFe}_2\text{O}_4$  nanoparticles is presented in Figure 2(c), which displays a type IV curve and H3 hysteresis. This demonstrates the prepared sample's predominance of mesoporous behavior ( $2\text{ nm} < \text{pore diameter} < 50\text{ nm}$ ) and the pores' a non-uniform distribution and connectivity. The BET specific surface area and total pore volume of  $\text{CaFe}_2\text{O}_4$  nanoparticles were found to be  $229.83\text{ m}^2/\text{g}$  and  $0.145\text{ cm}^3/\text{g}$ , respectively. The desorption isotherm was used to determine the pore size distributions of  $\text{CaFe}_2\text{O}_4$  nanoparticles (Figure 2(c) inset), and the average pore diameter was found to be  $\sim 2.5\text{ nm}$ . The adsorbent's PZC corresponds to the pH at which the adsorbent's net surface charge becomes zero. Figure 3(a) shows the variance of pH as a function of beginning pH, revealing that the PZC value of  $\text{CaFe}_2\text{O}_4$  nanoparticle is  $5.15$ . It signifies that the surface of the nanoparticle is positively charged when the pH is less than  $5.15$  and negatively charged when the pH is greater than  $5.15$ .

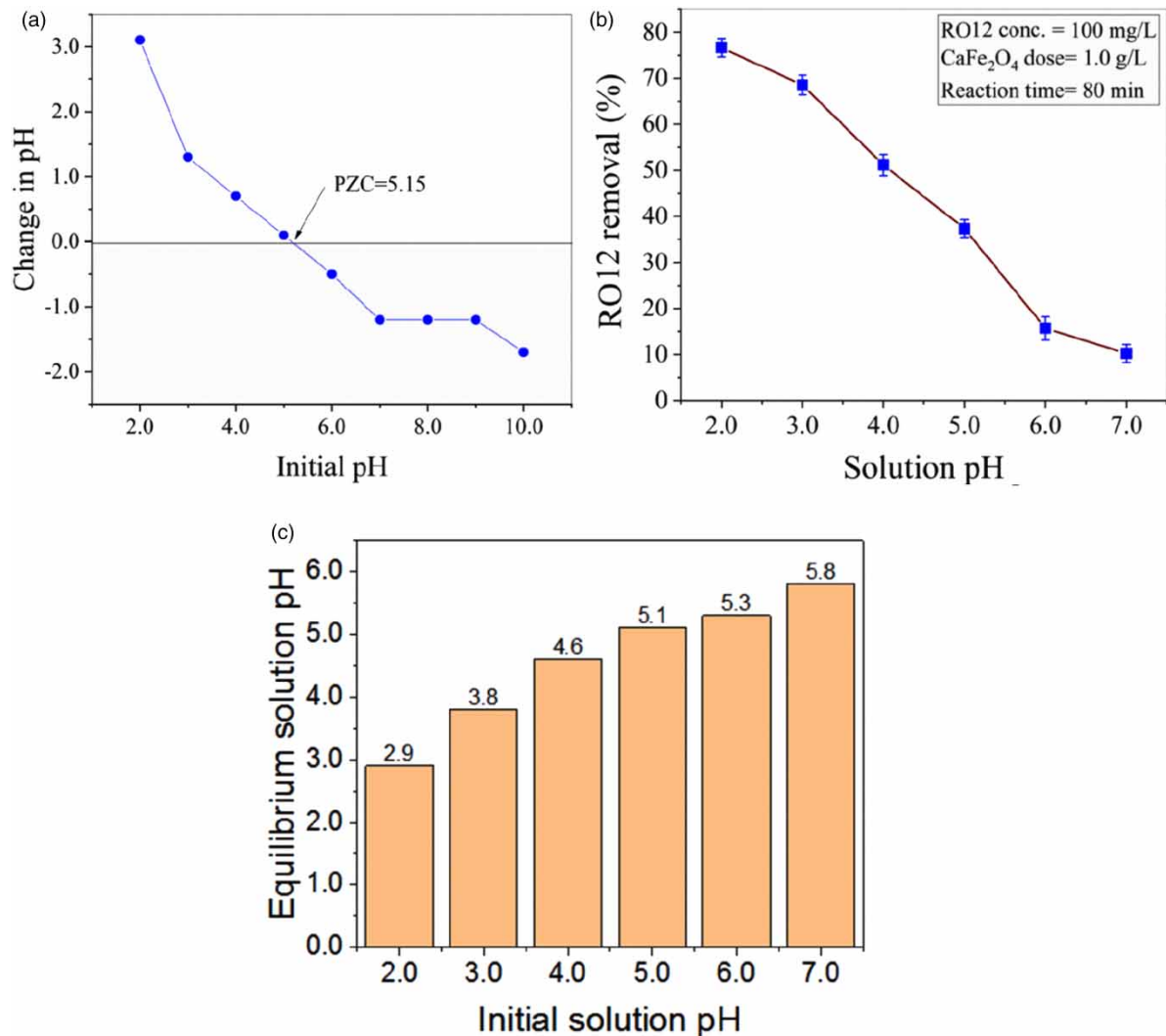
### 3.2. Effect of solution pH

Figure 3(b) shows the variation in RO12 removal (%) as a function of solution pH with the experimental conditions. At a solution pH of  $2.0$ , the adsorption process was preferred, and the highest removal efficiency of  $77\%$  was attained. The removal efficiency decreased consistently with rise of solution pH and only  $10.22\%$  removal is observed at solution pH  $7.0$ . Therefore, solution pH  $2.0$  was considered as the optimum pH for further adsorption studies. The equilibrium solution pH in relation to initial solution pH for this adsorption process is also incorporated in Figure 3(c). It can be observed that for the initial solution pH in the range of  $2.0$  to  $5.0$ , the equilibrium pH has increased from its initial value, however for the initial solution pH from  $6.0$  and above, the equilibrium pH has shown declining trend. This could be related to the PZC of  $\text{CaFe}_2\text{O}_4$  nanoparticles, which is found to be  $5.15$  (Figure 3(a)).

In the solution, the interaction of RO12 with the  $\text{CaFe}_2\text{O}_4$  is a complex process as this interaction involves the  $\text{H}^+$ ,  $\text{Cl}^-$ ,  $\text{Na}^+$  and anionic dye component present in the solution. In the dye and adsorbent mixed solution, when HCl was added to adjust the solution pH at  $2.0$ , the  $\text{H}^+$  interacted with the adsorbent leaving behind a large number of  $\text{Cl}^-$  present in the solution. The free  $\text{Cl}^-$  available in the solution help the complex RO12 molecule to be dissociated resulting to liberating  $\text{Na}^+$  in the solution. This creates the opportunity to the anionic RO12 component to interact with the protonated adsorbent present in the solution. The positively charged surface of  $\text{CaFe}_2\text{O}_4$  nanoparticles at solution pH  $2.0$  is also supported by the PZC measurement as PZC of  $\text{CaFe}_2\text{O}_4$  nanoparticles was found to be  $5.15$ . Similar adsorption behavior of RO12 have been reported by different research works (Ghaedi *et al.* 2011, 2013; Nia *et al.* 2014) indicating maximum RO12 uptake at highly acidic pH on account of strong electrostatic interaction between anionic component of RO12 and the protonated adsorbent surface. On the contrary,  $\text{CaFe}_2\text{O}_4$  nanoparticles surface become negative above solution pH  $5.15$ , causing the

**Table 1** | Details of FTIR spectrum of the  $\text{CaFe}_2\text{O}_4$  nanoparticles

Samples	IR region or bands ( $\text{cm}^{-1}$ )	Descriptions of bands
$\text{CaFe}_2\text{O}_4$ nanoparticles	3,454	(O-H) stretching
	1,634	(O-H) scissor bending
	1,421	(C - H) bending vibrations
	1,064	(Fe-Ca) stretching
	875	(Fe-O-H) bending vibrations
	712	(Fe-O) stretching
	624	(Fe-O) stretching
	566	(Fe - O) stretching vibrations
	526	(Ca-O) stretching vibrations
	495	(Ca-O) stretching vibrations
	451	(Fe-O) stretching



**Figure 3** | (a) PZC of CaFe<sub>2</sub>O<sub>4</sub> nanoparticles in the pH range 2.0–10.0, (b) variation of RO12 uptake efficiency (%) as a function of initial solution pH, (c) equilibrium solution pH as a function of initial solution pH for RO12 dye adsorption.

repulsion between anionic dye and negatively charged adsorbent surface. Furthermore at that pH, escalation of OH<sup>-</sup> result to competitive adsorption with the anionic dye species available in the system resulting to significant decrease in removal efficiency (Asim *et al.* 2019). The electrostatic interaction between the protonated CaFe<sub>2</sub>O<sub>4</sub> nanoparticles surface and RO12 at highly acidic condition is graphically exemplified in Figure 4.

### 3.3. Effect of CaFe<sub>2</sub>O<sub>4</sub> nanoparticles dose

The variation of RO12 removal (%) and adsorption capacity in relation to CaFe<sub>2</sub>O<sub>4</sub> nanoparticles dose is presented in Figure 5. With the increase in dose from 0.125 g/L to 1.0 g/L, dye removal (%) rose from 24.54% to 95.67%, and subsequent increase in adsorbent dose could not improve dye adsorption efficiency significantly. Quick increase in uptake efficiency with increasing adsorbent dose corresponds to greater surface area with higher adsorption sites at higher CaFe<sub>2</sub>O<sub>4</sub> nanoparticles dose. On the contrary, the adsorption capacity (mg/g) decreases from 157.06 mg/g to 52.14 mg/g with the increase in adsorbent dose from 0.125 g/L to 1.5 g/L. This may be due to (i) unsaturated active sites at higher dose, and (ii) overlapping of active adsorption sites on the surface of adsorbent; resulting to reduced adsorption capacity at higher dose (Sheela *et al.* 2012).

### 3.4. Effect of initial RO12 concentration and contact time

The variation of RO12 uptake efficiency (%) and adsorption capacity (mg/g) in relation to RO12 concentration (20.0–150.0 mg/L) with fixed CaFe<sub>2</sub>O<sub>4</sub> nanoparticles dose (1.0 g/L) have been displayed in Figure 6(a). More than 97% of RO12 removal was observed for lower dye concentrations (20–60 mg/L); though increase in dye



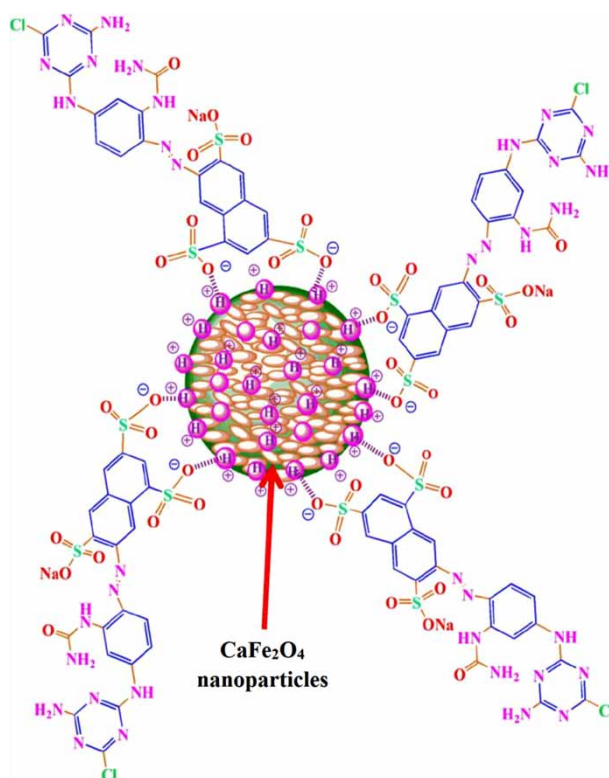


**Figure 4** | Schematic illustration of electrostatic interaction between protonated  $\text{CaFe}_2\text{O}_4$  nanoparticle surface and anionic RO12 dye species.

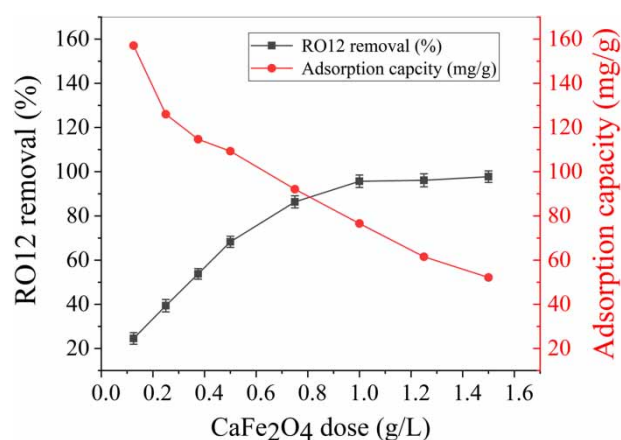


**Figure 5** | The effect of  $\text{CaFe}_2\text{O}_4$  nanoparticles dose on RO12 removal (%) and adsorption capacity (mg/g).

concentration reduced the removal efficiency gradually. The adsorption capacity was increased from 19.82–73.17 mg/g with enhancement in dye concentration from 20–80 mg/L, thereafter further increases in dye concentration have shown insignificant improvement in adsorption capacity. This may be due to the fact that at lower dye concentrations there were unsaturated active sites instead of high removal efficiency, but at higher dye concentrations all the active sites may get saturated and adsorption capacity reached equilibrium (Maleki *et al.* 2015).

The variation of RO12 removal (%) as a function of contact time is shown in Figure 6(b), which clearly depicts that initially the rate of adsorption was fast and the dye uptake efficiency increases with increasing contact time. Thereafter the adsorption rate was reduced and finally it reached equilibrium. This may be explained by the fact that, initially, availability of protonated  $\text{CaFe}_2\text{O}_4$  nanoparticles surface led to rapid adsorption of anionic dye species due to electrostatic attraction in highly acidic conditions. As the time increases, the electrostatic repulsion

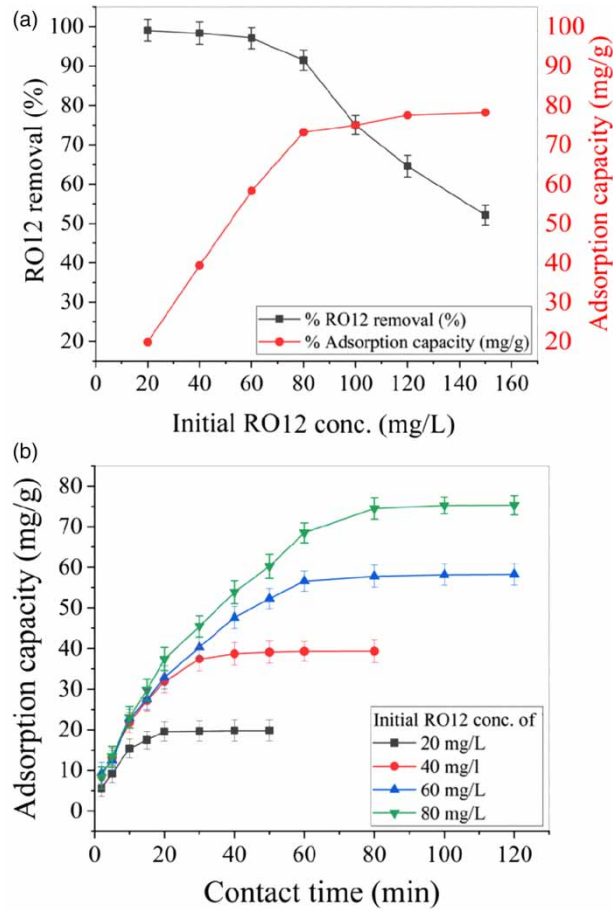


**Figure 6** | (a) The variation of RO12 removal (%) and adsorption capacity (mg/g) of as a function of initial RO12 dye concentration and (b) the variation of RO12 dye adsorption capacity as a function of contact time at different initial RO12 dye concentration.

between the already adsorbed anionic dye species and available adsorbate in the solution reduced the pore diffusion rate of RO12 on to the bulk of the  $\text{CaFe}_2\text{O}_4$  nanoparticles (Fraga *et al.* 2018). However, the equilibrium time is different for different initial RO12 concentration. For instance, at lower initial dye concentrations (20 and 40 mg/L) the equilibrium reached after 40 min, whereas for higher initial dye concentrations (60 and 80 mg/L) it takes nearly 80 min to reach equilibrium. Hence, a stirring time of 80 min was taken as the optimal time in this adsorption process.

### 3.5. Kinetic and isotherm modeling

In this study, the kinetic modeling was performed using the three most commonly applied kinetic models, namely pseudo-first-order, pseudo-second-order and intra-particle diffusion model. The linear forms of three kinetic models are shown in Equations (6)–(8) respectively.

$$\log(Q_e - Q_t) = \log Q_e - \frac{k_f}{2.303} t \quad (6)$$

$$\frac{t}{Q_t} = \frac{1}{k_s Q_e^2} + \frac{1}{Q_e} t \quad (7)$$

$$Q_t = k_{id} t^{\frac{1}{2}} + c \quad (8)$$

In Equations (6)–(8),  $Q_e$  represents the equilibrium adsorption capacity (mg/g),  $Q_t$  indicates the adsorption capacity (mg/g) at time  $t$ , and  $k_f$ ,  $k_s$ , and  $k_{id}$  represent the rate constants of the pseudo-first-order, pseudo-second-order and intra-particle diffusion model, respectively. In the case of the pseudo-second-order kinetic model, the initial adsorption rate is represented by the parameter ‘ $h$ ’ (mg/g.min), which can be described as

$h = k_2 Q_e^2$ . The constant ' $c$ ' in the intra-particle diffusion model indicates the thickness of the boundary layer and the higher the value of ' $c$ ', the greater the effect of the boundary layer on the adsorption process (Bhowmik *et al.* 2017). Table 2 lists the key kinetic parameters derived from linear fitting of experimental data using three kinetic models for various initial RO12 concentrations. From Table 2, it can be seen that the  $R^2$  values (0.993–0.988) for the pseudo-second-order kinetic model are superior to that of the pseudo-first-order kinetic model (0.972–0.904). Moreover the comparison between the experimental  $Q_e(\text{exp})$  and model-predicted  $Q_e$  values also clearly indicates the close agreement between the experimental  $Q_e(\text{exp})$  and model-predicted  $Q_e$  values for the pseudo-second-order model. Figure 7(a)–7(c) show the linear fitting of experimental data using pseudo-first-order, pseudo-second-order, and intra-particle diffusion kinetic models for varying initial RO12 concentrations (20–80 mg/L). Figure 7(b) shows the perfect fitting of experimental data with the pseudo-second-order kinetic model. The above observations suggest the applicability of the pseudo-second-order kinetic model for this adsorption process and confirm the occurrence of chemisorption between RO12 molecules and  $\text{CaFe}_2\text{O}_4$  nanoparticles.

In the case of the intra-particle diffusion model, if the experimental data fitting line passes through the origin of the plot, it means that intra-particle diffusion is the only rate controlling step. On the contrary, if the experimental data fitting shows two linear stages, it indicates that the first line represents boundary layer diffusion while the second linear line indicates the intra-particle diffusion, and the intra-particle diffusion is not the only rate limiting step (Tanhai *et al.* 2015). Experimental data can be well matched to two stages with strong correlation coefficients ( $R^2$ : 0.982–0.998) using the linear form of the intra-particle diffusion model and none of them passes through the origin of the plot. This indicates the involvement of macropore diffusion followed by micropore diffusion and the intra-particle diffusion is not the only rate determining step in this process. The intercept ' $c$ ' is increasing with the increase in initial RO12 concentration, which indicates the involvement of the boundary layer effect. Therefore, it can be concluded that this adsorption process is governed by the boundary layer diffusion predominantly, with the involvement of intra-particle diffusion (Pirouz *et al.* 2015).

The equilibrium adsorption data of RO12 onto  $\text{CaFe}_2\text{O}_4$  nanoparticles were analyzed by the two most commonly adopted isotherm models, namely Langmuir and Freundlich. Table 3 shows the linear form of both models, as well as all of the isotherm parameters and  $R^2$  values calculated from their linear fitting, where  $Q_m$  represents the maximum adsorption capacity reflected by a complete monolayer (mg/g),  $b$  indicates the Langmuir constant or adsorption equilibrium constant (L/mg),  $K_F$  and  $n$  are Freundlich constants indicating the capacity parameter (mg/g) and empirical intensity parameter, respectively. According to  $R^2$  values (Table 3), it is clear that the adsorption equilibrium data is better fitted by the Langmuir model ( $R^2 = 0.997$ ) compared to the Freundlich model ( $R^2 = 0.805$ ), indicating a monolayer adsorption of RO12 onto  $\text{CaFe}_2\text{O}_4$  nanoparticles. A dimensionless equilibrium parameter  $R_L$  of the Langmuir model can be used to assess the favorability of the adsorption process,

**Table 2** | Kinetic parameters of RO12 dye adsorption onto  $\text{CaFe}_2\text{O}_4$  nanoparticles (adsorbent dose = 1.0 g/L and initial RO12 concentration = 20–80 mg/L)

Models	Equation	Parameters	Initial RO12 concentration (mg/L)			
			20	40	60	80
First order kinetic	$\log(Q_e - Q_t) = \log Q_e - \frac{k_f}{2.303} t$	$k_f \times 10^2$	19.23	11.65	6.28	6.35
		$Q_e$	25.89	56.22	81.47	137.40
		$R^2$	0.972	0.984	0.973	0.904
Second order kinetic	$\frac{t}{Q_t} = \frac{1}{k_s Q_e^2} + \frac{1}{Q_e} t$ $h = k_2 Q_{2e}^2$	$k_s \times 10^3$	8.65	2.40	0.81	0.34
		$Q_e$	22.42	45.24	66.67	97.08
		$R^2$	0.993	0.994	0.991	0.988
		$h$	4.35	4.90	3.60	3.24
Intra-particle diffusion	$Q_t = k_{id} t^{\frac{1}{2}} + c$	$k_{id1}$	4.73	7.43	7.77	9.59
		$R^2$	0.982	0.993	0.996	0.998
		$c_1$	−0.91	−2.21	−2.53	−6.76
		$k_{id2}$	0.102	0.226	0.518	0.413
		$R^2$	0.942	0.775	0.860	0.835
		$c_2$	19.11	37.42	52.82	70.91
Experimental value		$Q_e(\text{exp})$	19.81	39.34	58.26	75.32

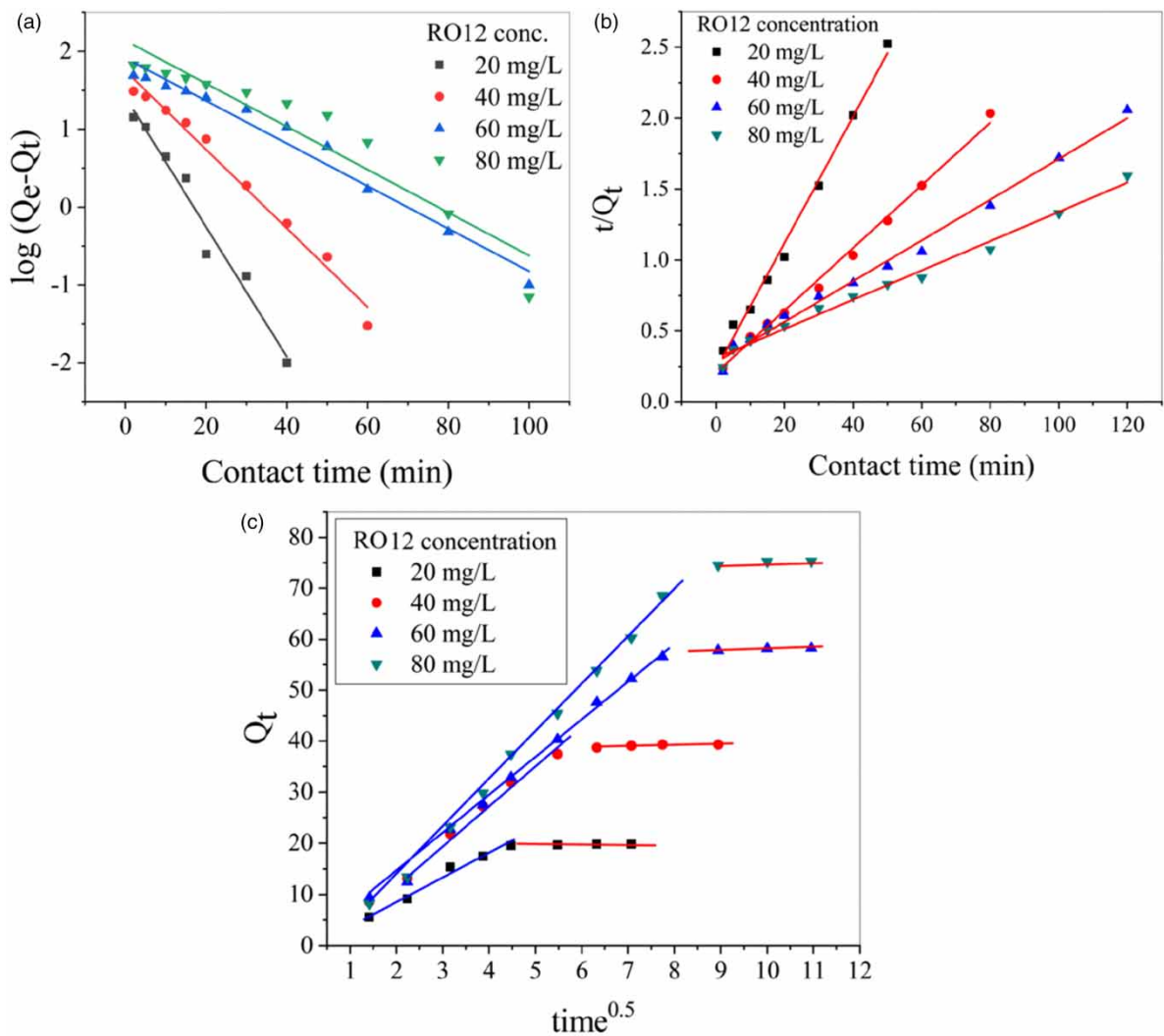


**Figure 7** | Plot showing the linear fitting of experimental data with (a) pseudo-first-order kinetic model, (b) pseudo-second-order kinetic model, and (c) intra-particle diffusion model for different initial RO12 dye concentrations.

**Table 3** | Adsorption equilibrium constants obtained from Langmuir and Freundlich isotherms fitting for adsorption of RO12 dye onto CaFe<sub>2</sub>O<sub>4</sub> nanoparticles

Isotherm	Linear form	Parameters	Values
Langmuir	$\frac{C_e}{Q_e} = \frac{1}{Q_m b} + \frac{C_e}{Q_m}$	$Q_m$ (mg/g)	276.92
		$b$ (L/mg)	5.65
		$R_L$	0.0087 – 0.0012
		$R^2$	0.997
Freundlich	$\ln Q_e = \ln K_F + \frac{1}{n} \ln C_e$	$n$	4.79
		$K_F$ (mg/g)	39.12
		$R^2$	0.805

which can be defined by Equation (9).

$$R_L = \left( \frac{1}{1 + b \cdot C_0} \right) \tag{9}$$

In this adsorption study, the calculated  $R_L$  values are between 0.0 to 1.0 and the Freundlich constant 'n' is more than 1.0 (Table 3), signifying the favorable adsorption of RO12 onto  $\text{CaFe}_2\text{O}_4$  nanoparticles. The maximum adsorption capacity of  $\text{CaFe}_2\text{O}_4$  nanoparticles towards RO12 was calculated from the Langmuir isotherm and found to be 276.92 mg/g. In terms of maximum adsorption capacity, the adsorptive performance of RO12 dye was compared to that of other earlier reported adsorbents in Table 4. It is clear that the fabricated  $\text{CaFe}_2\text{O}_4$  nanoparticles have exhibited higher or analogous adsorption capacity (276.92 mg/g) for RO12 compared to previously reported adsorbents like tin sulfide nanoparticles loaded on activated carbon (204.08 mg/g), platinum nanoparticles loaded on activated carbon (285.14 mg/g), ZnS:Mn nanoparticles loaded on activated carbon (94.52 mg/g) and copper sulfide nanoparticles-activated carbon (96.9 mg/g). Therefore, the above observation proposes the potential application of  $\text{CaFe}_2\text{O}_4$  nanoparticles for RO12 adsorption from aqua matrix.

### 3.6. Thermodynamic study

To explore the effect of reaction temperature on the adsorption process of RO12 onto  $\text{CaFe}_2\text{O}_4$  nanoparticles, the standard enthalpy change ( $\Delta H^0$ ), standard entropy change ( $\Delta S^0$ ), and standard Gibbs free energy change ( $\Delta G^0$ ) were determined from the following equations:

$$\Delta G^0 = -RT \ln k_c \quad (10)$$

$$\ln k_c = \frac{\Delta S^0}{R} - \frac{\Delta H^0}{RT} \quad (11)$$

$$k_c = \frac{Q_e}{C_e} \quad (12)$$

where,  $k_c$  represents the distribution coefficient,  $R$  = gas constant ( $0.008314 \text{ kJ mol}^{-1} \text{ K}^{-1}$ );  $T$  = temperature in Kelvin (K). The values of  $\Delta H^0$  and  $\Delta S^0$  were determined from the slope and intercept of the plot of  $\ln k_c$  versus  $1/T$ , respectively. The calculated thermodynamic parameters are shown in Table 5, from which it is clear that all the  $\Delta G^0$  values are negative and a shift of  $\Delta G^0$  is observed from  $-8.76$  to  $-3.19 \text{ kJ/mol}$  with increasing temperature from  $27^\circ\text{C}$  to  $55^\circ\text{C}$ . This confirms that the process is spontaneous in the considered temperature range and at the lower temperature the process is rapid and more spontaneous. The calculated  $\Delta H^0$  value ( $-71.86 \text{ kJ mol}^{-1} \text{ K}^{-1}$ ) confirmed that the adsorption process is exothermic in nature which is accordance with the decreasing adsorption capacity with an increasing reaction temperature. The calculated  $\Delta H^0$  value is more than  $40 \text{ kJ/mol}$ , which imply that the process is occurring predominantly by chemisorption. The negative value of  $\Delta S^0$  ( $-211.475 \text{ J/mole.K}$ ) corresponds to a decrease in degree of freedom of the RO12 species and suggest the decrease in concentration of RO12 in solid-solution interface indicating thereby increase in RO12 onto the solid phase. This is the usual effect of the chemisorption process (Bhowmik *et al.* 2016).

### 3.7. RO12 removal (%) prediction modeling by ANN

The data from the RO12 adsorption experiments were utilized to train the neural networks so as to determine the optimal network for accurate prediction of RO12 dye removal (%). Efficiency of the ANN model was analyzed in terms of  $R^2$  value maximization and MSE value minimization while changing the numbers of nodes in hidden layer from 1 to 30. The dependence of MSE,  $R^2$  values and number of epochs with neuron numbers (1 – 30) at the hidden layer for ANN model development is depicted in Table 6. It is clear from Table 6 that with an increase in the number of neurons, the MSE values have reduced gradually and a network with 7 numbers of neurons at hidden layer

**Table 4** | Comparison in terms of maximum adsorption capacity of  $\text{CaFe}_2\text{O}_4$  nanoparticles with other reported adsorbents for RO12 dye

Adsorbent	Maximum adsorption capacity (mg/g)	Reference
Tin sulfide nanoparticles loaded on activated carbon	204.08	Ghaedi <i>et al.</i> (2013)
Platinum nanoparticles loaded on activated carbon	285.143	Ghaedi <i>et al.</i> (2011)
ZnS:Mn nanoparticles loaded on activated carbon	94.52	Hajati <i>et al.</i> (2014)
Copper sulfide nanoparticles-activated carbon	96.9	Ghaedi <i>et al.</i> (2014)
$\text{CaFe}_2\text{O}_4$ nanoparticles	276.92	This study



**Table 5** | Thermodynamic parameters for RO12 dye adsorption onto  $\text{CaFe}_2\text{O}_4$  nanoparticles

$\Delta H^\circ$ (KJ/mol)	$\Delta S^\circ$ (J/mol.K)	$\Delta G^\circ$ (KJ/mol)				
		300.15 K	308.15 K	313.15 K	318.15 K	328.15 K
-71.86	-211.475	-8.76	-6.92	-5.00	-3.86	-3.19

**Table 6** | Dependence of MSE,  $R^2$  value, and number of epochs with neuron numbers (1–30) at the hidden layer for ANN model development with LM algorithm

Number of neurons	MSE	$R^2$			Number of epochs
		Training	Testing	Validation	
1	0.01490	0.849	0.633	0.830	8
2	0.01000	0.963	0.963	0.959	20
3	0.00750	0.979	0.947	0.977	33
4	0.00470	0.975	0.967	0.979	745
5	0.00280	0.973	0.979	0.977	27
6	0.00219	0.943	0.905	0.981	13
7	<b>0.00185</b>	<b>0.987</b>	<b>0.985</b>	<b>0.981</b>	<b>246</b>
8	0.00294	0.991	0.92	0.971	209
9	0.00296	0.983	0.989	0.985	11
10	0.00297	0.993	0.789	0.985	42
11	0.00299	0.991	0.973	0.975	22
12	0.00313	0.989	0.973	0.979	75
13	0.00230	0.989	0.973	0.981	18
14	0.00343	0.983	0.951	0.973	5
15	0.00344	0.963	0.967	0.985	8
16	0.00351	0.983	0.922	0.971	51
17	0.00470	0.983	0.979	0.975	56
18	0.00516	0.993	0.975	0.963	18
20	0.00730	0.987	0.961	0.989	41
25	0.00750	0.975	0.943	0.957	23
30	0.02160	0.928	0.932	0.838	18

shown the minimum MSE of 0.00185 and high  $R^2$  values of 0.987, 0.985, and 0.981 for the training, testing and validation data set, respectively. Hence, network with 7 neurons in the hidden layer is selected as the optimal one and can be represented as 4–7–1. The optimal network has shown the best validation performance at epoch 246 and thereafter no improvement is seen with increase in numbers of epochs, which is depicted in [Figure 8\(a\)](#). The linear regression analysis between model predicted normalized values and normalized experimental values ([Figure 8\(b\)](#)) has shown very good agreement among them and a very high linear regression coefficient is observed (0.986). The weight and bias values of hidden and output layer as determined from the optimum network are shown in [Table 7](#), which were used for performing the sensitivity analysis to determine the relative importance of four input parameters onto the output parameter (RO12 removal efficiency). The analysis was performed employing Equation (5), and it was observed that the input parameter solution pH has evolved as the most critical parameter with a relative importance of 42%.  $\text{CaFe}_2\text{O}_4$  nanoparticles dose and initial RO12 concentration have shown the moderate importance of 27 and 22% respectively, whereas the input parameter contact time is the least important input parameter with a relative importance of only 9%. The sensitivity analysis results are in agreement with experimental data as RO12 removal efficiency was very sensitive to solution pH ([Figure 3\(b\)](#)), whereas the dye uptake efficiency was hardly affected by contact time, once the adsorption process reaches equilibrium.

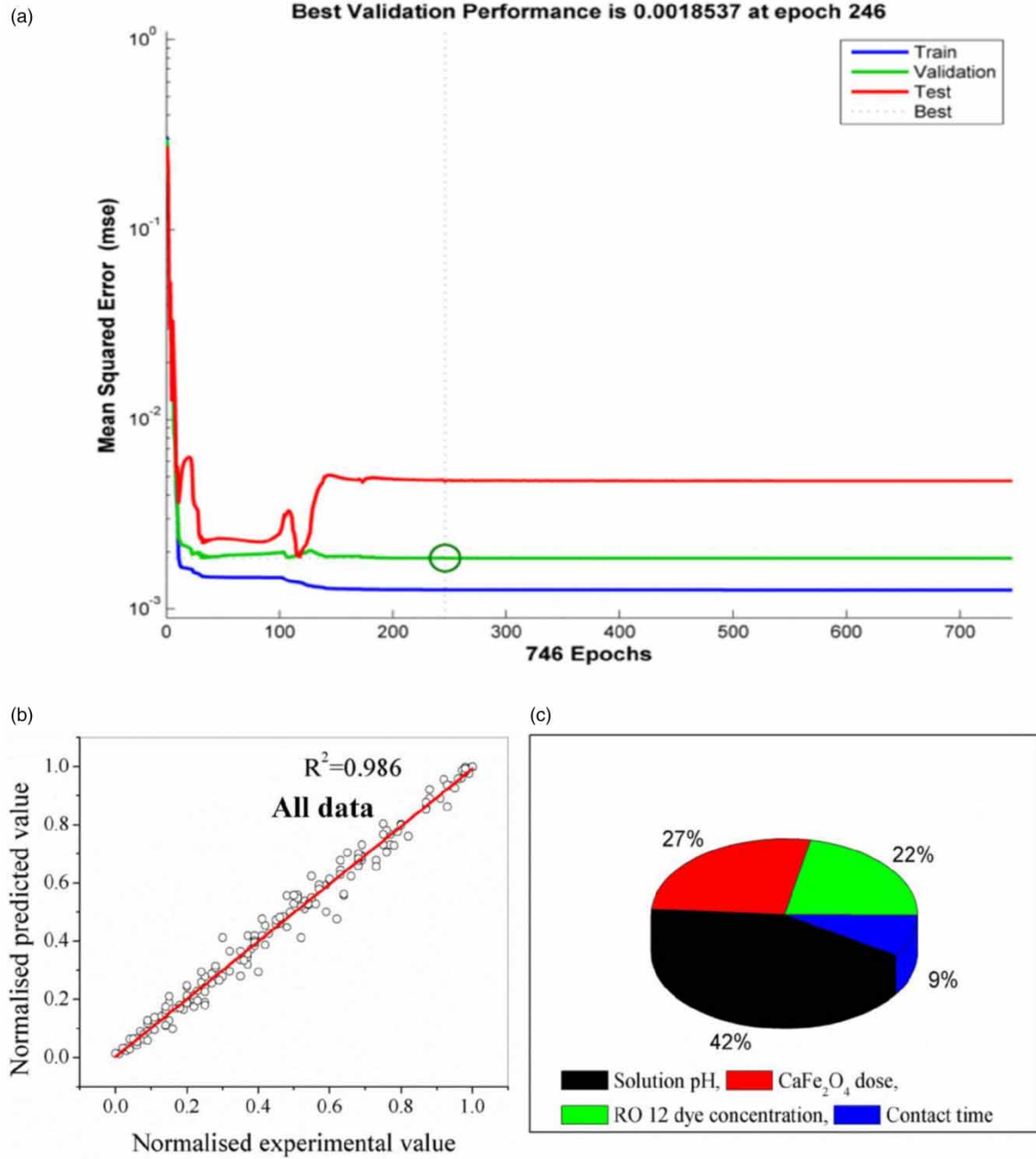


**Figure 8** | (a) The effect of numbers of epochs on the validation performance of the optimal network in terms of MSE, (b) the ANN model predicted vs. experimental data for RO12 dye adsorption, and (c) the relative importance of input variables on RO12 dye removal efficiency.

**Table 7** | The weight and bias values of each layer determined using the optimum ANN network

IW(1,1)				LW(2,1)	b(1)	b(2)
0.052824	0.095193	-0.83673	3.0077;	[-9.228	[2.9502;	[-2.8552]
0.39011	-0.30296	1.8046	0.58119;	-10.2692	-0.61921;	
-6.0722	-0.70881	-0.40279	-1.6931;	-5.4792	-6.976;	
0.57926	-4.7498	-0.065921	3.8396;	-2.4104	-3.5055;	
0.37183	-0.12937	1.7755	0.40356;	10.4269	-0.46498;	
-0.35711	-4.0593	-0.15297	-4.7005;	2.8672	0.15203;	
-0.056379	-0.040115	-3.3043	0.35331]	-7.517]	-4.9392]	

#### 4. CONCLUSIONS

This investigation shows the successful synthesis of magnetically separable crystalline  $\text{CaFe}_2\text{O}_4$  nanoparticles and its potential use as an adsorbent for removing an anionic dye called RO12 from an aqueous medium. The most efficient dye removal was observed under very acidic condition ( $\text{pH} = 2.0$ ) and electrostatic attraction between anionic RO12 and the protonated surface of  $\text{CaFe}_2\text{O}_4$  nanoparticles was the main driving force behind this adsorption process. The Langmuir isotherm model is well suited to the experimental data and maximum adsorption capacity of 276.92 mg/g is determined from this model. Kinetic analysis confirmed the applicability of the pseudo-second-order kinetic model in conjunction with the intra-particle diffusion model. The thermodynamic analysis revealed that this adsorption process is spontaneous and exothermic in nature in the considered temperature range. An optimal ANN model (4–7–1) was developed successfully for prediction of RO12 (%) with a high  $R^2$  value of 0.986 and very low MSE of 0.00185. The developed ANN model could efficiently predict the RO12 dye removal (%) using the adsorption experimental data. Therefore, in the context of high demand for dye-loaded industrial effluent treatment, the fabricated  $\text{CaFe}_2\text{O}_4$  nanoparticles may find their application owing to their easy magnetic separation, environmentally friendly nature, and high adsorption capacity towards RO12.

#### DATA AVAILABILITY STATEMENT

All relevant data are included in the paper or its Supplementary Information.

#### REFERENCES

- Al-Anazi, A., Abdelraheem, W. H., Han, C., Nadagouda, M. N., Sygellou, L., Arfanis, M. K., Falaras, P., Sharma, V. K. & Dionysiou, D. D. 2018 Cobalt ferrite nanoparticles with controlled composition-peroxymonosulfate mediated degradation of 2-phenylbenzimidazole-5-sulfonic acid. *Applied Catalysis B: Environmental* **221**, 266–279.
- Al-Anazi, A., Abdelraheem, W. H., Scheckel, K., Nadagouda, M. N., OShea, K. & Dionysiou, D. D. 2020 Novel franklinite-like synthetic zinc-ferrite redox nanomaterial: synthesis, and evaluation for degradation of diclofenac in water. *Applied Catalysis B: Environmental* **275**, 119098.
- Asim, T., Mamoon, M., Tahir, A., Nisar, N., Ali, A. & Sheikh, A. 2019 Alumina as environmentally stable adsorbent for the removal of dyes from waste water. *Water Practice and Technology* **14**(1), 62–70.
- Berchmans, L. J., Myndyk, M., Da Silva, K. L., Feldhoff, A., Subrt, J., Heitjans, P., Becker, K. D. & Sepelak, V. 2010 A rapid one-step mechanosynthesis and characterization of nanocrystalline  $\text{CaFe}_2\text{O}_4$  with orthorhombic structure. *Journal of Alloys and Compounds* **500**(1), 68–73.
- Bhowmik, K. L., Debnath, A., Nath, R. K., Das, S., Chattopadhyay, K. K. & Saha, B. 2016 Synthesis and characterization of mixed phase manganese ferrite and hausmannite magnetic nanoparticle as potential adsorbent for methyl orange from aqueous media: artificial neural network modeling. *Journal of Molecular Liquids* **219**, 1010–1022.
- Bhowmik, K. L., Debnath, A., Nath, R. K. & Saha, B. 2017 Synthesis of  $\text{MnFe}_2\text{O}_4$  and  $\text{Mn}_3\text{O}_4$  magnetic nano-composites with enhanced properties for adsorption of Cr (VI): artificial neural network modeling. *Water Science and Technology* **76**(12), 3368–3378.
- Bhowmik, M., Deb, K., Debnath, A. & Saha, B. 2018 Mixed phase  $\text{Fe}_2\text{O}_3/\text{Mn}_3\text{O}_4$  magnetic nanocomposite for enhanced adsorption of methyl orange dye: neural network modeling and response surface methodology optimization. *Applied Organometallic Chemistry* **32**(3), e4186.
- Bhowmik, M., Kanmani, M., Debnath, A. & Saha, B. 2019 Sono-assisted rapid adsorption of anionic dye onto magnetic  $\text{CaFe}_2\text{O}_4/\text{MnFe}_2\text{O}_4$  nanocomposite from aqua matrix. *Powder Technology* **354**, 496–504.
- Bhowmik, M., Debnath, A. & Saha, B. 2020 Fabrication of mixed phase  $\text{CaFe}_2\text{O}_4$  and  $\text{MnFe}_2\text{O}_4$  magnetic nanocomposite for enhanced and rapid adsorption of methyl orange dye: statistical modeling by neural network and response surface methodology. *Journal of Dispersion Science and Technology* **41**(13), 1937–1948.
- Caner, N., Sari, A. & Tuzen, M. 2015 Adsorption characteristics of mercury (II) ions from aqueous solution onto chitosan-coated diatomite. *Industrial & Engineering Chemistry Research* **54**(30), 7524–7533.
- Chafi, M., Gourich, B., Essadki, A. H., Vial, C. & Fabregat, A. 2011 Comparison of electrocoagulation using iron and aluminium electrodes with chemical coagulation for the removal of a highly soluble acid dye. *Desalination* **281**, 285–292.
- Chen, Z., Zhang, J., Fu, J., Wang, M., Wang, X., Han, R. & Xu, Q. 2014 Adsorption of methylene blue onto poly (cyclotriphosphazene-co-4, 4'-sulfonyldiphenol) nanotubes: kinetics, isotherm and thermodynamics analysis. *Journal of Hazardous Materials* **273**, 263–271.
- Cui, D., Guo, Y. Q., Cheng, H. Y., Liang, B., Kong, F. Y., Lee, H. S. & Wang, A. J. 2012 Azo dye removal in a membrane-free up-flow biocatalyzed electrolysis reactor coupled with an aerobic bio-contact oxidation reactor. *Journal of Hazardous Materials* **239**, 257–264.
- Deb, A., Kanmani, M., Animesh, D., Bhowmik, K. L. & Biswajit, S. 2017 Preparation and characterization of magnetic  $\text{CaFe}_2\text{O}_4$  nanoparticles for efficient adsorption of toxic Congo Red dye from aqueous solution: predictive modeling by artificial neural network. *Desalination and Water Treatment* **89**, 197–209.

- Debnath, A. & Chakraborty, S. 2013 Experimental design to optimise colour removal of diazo dye Congo Red using Zero-Valent Iron. *International Journal of Environment and Waste Management* **11**(3), 267–288.
- Debnath, A., Thapa, R., Chattopadhyay, K. K. & Saha, B. 2015 Spectroscopic studies on interaction of Congo red with ferric chloride in aqueous medium for wastewater treatment. *Separation Science and Technology* **50**(11), 1684–1688.
- Deng, J., Shao, Y. S. & Gao, N. Y. 2013  $\text{CoFe}_2\text{O}_4$  magnetic nanoparticles as a highly active heterogeneous catalyst of oxone for the degradation of diclofenac in water. *Journal of Hazardous Materials* **262**, 836–844.
- Fraga, T. J. M., dos Santos Marques Fraga, D. M., da Silva, T. C., Carvalho, M. N. & da Motta Sobrinho, M. A. 2018 Adsorption of reactive dyes onto thermally treated waste from aluminum lamination. *Water Practice & Technology* **13**(3), 629–641.
- Ghaedi, M., Tashkhourian, J., Pebdani, A. A., Sadeghian, B. & Ana, F. N. 2011 Equilibrium, kinetic and thermodynamic study of removal of Reactive orange 12 on platinum nanoparticle loaded on activated carbon as novel adsorbent. *Korean Journal of Chemical Engineering* **28**(12), 2255–2261.
- Ghaedi, M., Karimi, F., Barazesh, B., Sahraei, R. & Daneshfar, A. 2013 Removal of Reactive Orange 12 from aqueous solutions by adsorption on tin sulfide nanoparticle loaded on activated carbon. *Journal of Industrial and Engineering Chemistry* **19**(3), 756–763.
- Ghaedi, M., Ghaedi, A. M., Abdi, F., Roosta, M., Sahraei, R. & Daneshfar, A. 2014 Principal component analysis-artificial neural network and genetic algorithm optimization for removal of Reactive orange 12 by copper sulfide nanoparticles-activated carbon. *Journal of Industrial and Engineering Chemistry* **20**(3), 787–795.
- Gupta, V. K., Pathania, D., Agarwal, S. & Singh, P. 2012 Adsorptional photocatalytic degradation of methylene blue onto pectin–CuS nanocomposite under solar light. *Journal of Hazardous Materials* **243**, 179–186.
- Hajati, S., Ghaedi, M., Karimi, F., Barazesh, B., Sahraei, R. & Daneshfar, A. 2014 Competitive adsorption of direct yellow 12 and reactive orange 12 on ZnS: Mn nanoparticles loaded on activated carbon as novel adsorbent. *Journal of Industrial and Engineering Chemistry* **20**(2), 564–571.
- He, A., Lu, R., Wang, Y., Xiang, J., Li, Y. & He, D. 2017 Adsorption characteristic of Congo red onto magnetic  $\text{MgFe}_2\text{O}_4$  nanoparticles prepared via the solution combustion and gel calcination process. *Journal of Nanoscience and Nanotechnology* **17**(6), 3967–3974.
- Khanna, L. & Verma, N. K. 2013 PEG/ $\text{CaFe}_2\text{O}_4$  nanocomposite: structural, morphological, magnetic and thermal analyses. *Physica B: Condensed Matter* **427**, 68–75.
- Khanna, L. & Verma, N. K. 2014 Biocompatibility and superparamagnetism in novel silica/ $\text{CaFe}_2\text{O}_4$  nanocomposite. *Materials Letters* **128**, 376–379.
- Konicki, W., Sibera, D., Mijowska, E., Lendzion-Bieluń, Z. & Narkiewicz, U. 2013 Equilibrium and kinetic studies on acid dye Acid Red 88 adsorption by magnetic  $\text{ZnFe}_2\text{O}_4$  spinel ferrite nanoparticles. *Journal of Colloid and Interface Science* **398**, 152–160.
- Kooh, M. R. R., Dahri, M. K., Lim, L. B., Lim, L. H. & Malik, O. A. 2016 Batch adsorption studies of the removal of methyl violet 2B by soya bean waste: isotherm, kinetics and artificial neural network modelling. *Environmental Earth Sciences* **75**(9), 783.
- Kumari, M., Pittman, C. U. & Mohan, D. 2015 Heavy metals [chromium (VI) and lead (II)] removal from water using mesoporous magnetite ( $\text{Fe}_3\text{O}_4$ ) nanospheres. *Journal of Colloid and Interface Science* **442**, 120–132.
- Li, X., Hou, Y., Zhao, Q. & Wang, L. 2011 A general, one-step and template-free synthesis of sphere-like zinc ferrite nanostructures with enhanced photocatalytic activity for dye degradation. *Journal of Colloid and Interface Science* **358**(1), 102–108.
- Liu, S. Q., Feng, L. R., Xu, N., Chen, Z. G. & Wang, X. M. 2012 Magnetic nickel ferrite as a heterogeneous photo-Fenton catalyst for the degradation of rhodamine B in the presence of oxalic acid. *Chemical Engineering Journal* **203**, 432–439.
- Liu, X., Zhang, Z., Shi, W., Zhang, Y., An, S. & Zhang, L. 2015 Adsorbing properties of magnetic nanoparticles Mn-ferrites on removal of Congo red from aqueous solution. *Journal of Dispersion Science and Technology* **36**(4), 462–470.
- Maleki, A., Hayati, B., Naghizadeh, M. & Joo, S. W. 2015 Adsorption of hexavalent chromium by metal organic frameworks from aqueous solution. *Journal of Industrial and Engineering Chemistry* **28**, 211–216.
- Montoya-Suarez, S., Colpas-Castillo, F., Meza-Fuentes, E., Rodríguez-Ruiz, J. & Fernandez-Maestre, R. 2016 Activated carbons from waste of oil-palm kernel shells, sawdust and tannery leather scraps and application to chromium (VI), phenol, and methylene blue dye adsorption. *Water Science and Technology* **73**(1), 21–27.
- Nia, R. H., Ghaedi, M. & Ghaedi, A. M. 2014 Modeling of reactive orange 12 (RO 12) adsorption onto gold nanoparticle-activated carbon using artificial neural network optimization based on an imperialist competitive algorithm. *Journal of Molecular Liquids* **195**, 219–229.
- Pirouz, M. J., Beyki, M. H. & Shemirani, F. 2015 Anhydride functionalised calcium ferrite nanoparticles: a new selective magnetic material for enrichment of lead ions from water and food samples. *Food Chemistry* **170**, 131–137.
- Sheela, T., Nayaka, Y. A., Viswanatha, R., Basavanna, S. & Venkatesha, T. G. 2012 Kinetics and thermodynamics studies on the adsorption of Zn (II), Cd (II) and Hg (II) from aqueous solution using zinc oxide nanoparticles. *Powder Technology* **217**, 163–170.
- Singh, N. H., Kezo, K., Debnath, A. & Saha, B. 2018 Enhanced adsorption performance of a novel Fe-Mn-Zr metal oxide nanocomposite adsorbent for anionic dyes from binary dye mix: response surface optimization and neural network modeling. *Applied Organometallic Chemistry* **32**(3), e4165.

- Tanhaei, B., Ayati, A., Lahtinen, M. & Sillanpaa, M. 2015 Preparation and characterization of a novel chitosan/ $\text{Al}_2\text{O}_3$ /magnetite nanoparticles composite adsorbent for kinetic, thermodynamic and isotherm studies of methyl orange adsorption. *Chemical Engineering Journal* **259**, 1–10.
- Yang, Y., Lin, X., Wei, B., Zhao, Y. & Wang, J. 2014 Evaluation of adsorption potential of bamboo biochar for metal-complex dye: equilibrium, kinetics and artificial neural network modeling. *International Journal of Environmental Science and Technology* **11**(4), 1093–1100.
- Yao, Y., Cai, Y., Lu, F., Wei, F., Wang, X. & Wang, S. 2014 Magnetic recoverable  $\text{MnFe}_2\text{O}_4$  and  $\text{MnFe}_2\text{O}_4$ -graphene hybrid as heterogeneous catalysts of peroxymonosulfate activation for efficient degradation of aqueous organic pollutants. *Journal of Hazardous Materials* **270**, 61–70.
- Zeng, S., Duan, S., Tang, R., Li, L., Liu, C. & Sun, D. 2014 Magnetically separable  $\text{Ni}_0.6\text{Fe}_{2.4}\text{O}_4$  nanoparticles as an effective adsorbent for dye removal: synthesis and study on the kinetic and thermodynamic behaviors for dye adsorption. *Chemical Engineering Journal* **258**, 218–228.

First received 15 February 2021; accepted in revised form 25 June 2021. Available online 8 July 2021